Scatter correction for cone-beam computed tomography using self-adaptive scatter kernel superposition*

XIE Shi-Peng(谢世朋)[1,2] LUO Li-Min(罗立民)[2]

[1] School of Mathematical Sciences, Anhui University, Hefei 230039, China
[2] School of Computer Science & Engineering, Southeast University, Nanjing 210096, China

Abstract: The authors propose a combined scatter reduction and correction method to improve image quality in cone beam computed tomography (CBCT). The scatter kernel superposition (SKS) method has been used occasionally in previous studies. However, this method differs in that a scatter detecting blocker (SDB) was used between the X-ray source and the tested object to model the self-adaptive scatter kernel. This study first evaluates the scatter kernel parameters using the SDB, and then isolates the scatter distribution based on the SKS. The quality of image can be improved by removing the scatter distribution. The results show that the method can effectively reduce the scatter artifacts, and increase the image quality. Our approach increases the image contrast and reduces the magnitude of cupping. The accuracy of the SKS technique can be significantly improved in our method by using a self-adaptive scatter kernel. This method is computationally efficient, easy to implement, and provides scatter correction using a single scan acquisition.

Key words: scatter correction, Compton scatter, cone beam computed tomography

PACS: 87.57.ue **DOI:** 10.1088/1674-1137/36/6/015

1 Introduction

X-ray systems with a large area detectors, as commonly used for cone beam computed tomography (CBCT), are more susceptible to scatter-related artifacts. To alleviate this problem, various correction methods using software-based [1–12], hardware-based [13–18], or combined hybrid approaches [19–23] have been proposed in the literature.

Hardware-based scatter suppressing techniques include increasing the air gap [16], using an anti-scatter grid [17], applying the bowtie method [18], and so on. However, these techniques can eliminate only part of the scattered radiation. Therefore, more efforts are being made toward scatter correction, namely removing the scatter fluence from scatter-contaminated projections.

Different correction strategies have been proposed using software-based methods, such as the scatter kernel calculation [6, 7, 10, 12], analytical computation [1, 4, 5, 11], and Monte Carlo (MC) simulation [8, 9]. Generally speaking, the model in the analytical scheme is usually regular in geometry and homogeneous in radiation properties [11], and thus the estimated scatter may not reflect the real situation. Scatter estimation from Monte Carlo simulation is accurate if the information on the scattering medium is known from, for example, CBCT. However, the formidably heavy computation associated with Monte Carlo scatter estimation hinders its real life applications.

Combined hybrid approaches include primary modulation [23] and the scatter measurement method [13, 14]. The primary modulation method is impressive in theory. In this method, a part of the primary fluence is modulated to a high frequency. When it is demodulated, weighted and subtracted, the primary intensity is neutralized, while the scatter fluence remains. The proper parameter for optimal modulation is crucial in applying this method to prevent contamination between the modulated and original primary fluence, which is important for accuracy in density

Received 24 August 2011
* Supported by Graduate Student Research Foundation of Jiangsu Province (CX10B-079Z)

and spatial resolution. The scatter measurement method is based on the fact that scatter distribution in space is rather smooth, so it can be reconstructed by knowing the scatter in some regions. However, other types of noise and artifacts in the imaging system may cause difficulties in estimating the algorithm parameters needed for the reconstruction and thus result in either scatter under- or overcorrection, although the difficulty can be somewhat alleviated by adding more shaded regions.

In this work, we propose a blocker-based approach to simultaneously estimate the scatter signal. The measured signal in the blocked region is attributed to the scatter, and the scatter fluence of the projection data is estimated from the measured signal in the blocked region. Using the measured scatter, we can estimate the scatter kernel parameter, and then estimate the scatter distribution. Because the blocker is rotated one degree every time during CBCT data acquisition, a particular voxel within the field of view will not be always blocked in all projections. In this paper, we focus on the scatter correction of a projected image.

We conduct analytical and Roentgen simulations (Monte Carlo simulation [24]) of the entire scatter measurement procedure to assess the performance of our method by comparing it with the existing scatter kernel methods (Sun et al, [12]) (Section 3). The proposed methods are discussed in Section 4 and conclusions are drawn in the last section.

2 Materials and methods

2.1 The basic concept and implementation

Figure 1 illustrates the geometric setup of the scatter detecting blocker (SDB) used for CBCT imaging. The SDB consists of a cross (2 mm wide ×3 mm thick ×120 mm in length) made of lead strips, and supported by a plastic plate. The SDB is inserted between the X-ray source and the tested object, and rotates around its isocenter. In our experiments, the X-ray source, SDB, object-of-interest and the detector are placed along a determined direction, and the distances between the two adjacent objects are 230, 770, and 400 mm respectively.

In order to reduce the reconstruction error in a CBCT system, the projection data sets are collected after rotating the SDB by one degree, and not shade a particular voxel from view in all of the projections.

2.2 The scatter measurement procedure

The scatter correction algorithm for the modified system with the insertion of the SDB is divided into the following steps:

Step 1 Measure the signal in the blocked region, and use the signal to compute the scatter kernel parameter.

Step 2 Down-sample projection data.

Step 3 Make an initial scatter estimate.

Step 4 Compute primary estimate as the detector signal – scatter estimate.

Step 5 Convolve primary estimates with kernels to refine the scatter estimate.

Step 6 If not converged, go to Step 3.

Step 7 Up-sample final estimate.

Step 8 Compute the final primary estimate.

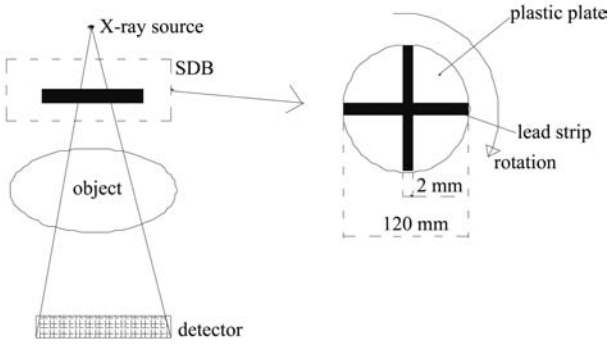

Fig. 1. Geometric configuration of the X-ray system with the insertion of the blocker.

2.3 The algorithm for scatter estimation

Lead strips are thick enough to almost completely block the incident X-ray beam. Inside the strip shadows, no primary signals are detected and the measured signals provide scatter samples. The partial scatter information is measured in the "shadow" regions beneath the lead septa for each projection image, imaging data are acquired simultaneously during partial scatter measurement. Assuming the insertion of the lead strips does not greatly perturb the shape of scatter distributions in the CBCT projection, scatter kernels can be derived from the partial scatter information.

The resulting scatter point spread functions (PSF) are fitted to the following model based on the approach of (Sun et al, [12]):

$$F_{\mathrm{psf}}(I_{\mathrm{p}}, I_0, r) = A(I_p/I_0)^{\alpha}(\ln(I_0/I_{\mathrm{p}}))^{\beta}[\exp(-r^2/2\sigma_1^2) + B\exp(-r^2/2\sigma_2^2)], \quad (1)$$

the spatial position $r = xi + yj$ is measured at the detector, I_{p} is the primary signal intensity, and I_0 is the unattenuated intensity value. The fitted parameters are α, β, A, B, σ_1, σ_2.

The scatter PSF described by Eq. (1) can be separated into an amplitude factor A_{f} and form function

$h_{\rm S}$. Thus, to generate the scatter estimate $I_{\rm S}(x,\ y)$ at position $(x,\ y)$, the convolution operation is written as a discrete summation:

$$I_{\rm S}(x,y) = \sum_{n=1}^{N}\sum_{m=1}^{M} I'_{\rm P}(x_m,y_n)A_{\rm f}(x_m,y_n)h_{\rm S} \times(x-x_m,y-y_n), \quad (2)$$

where $x_m,\ y_n$ are the pixel coordinates that span a matrix of size $M,\ N$. To increase computational efficiency, the pixel matrix used for scatter calculation can be a down-sampled version of the original projection matrix since the scatter PSF is composed of mainly low frequency content. $I'_{\rm p}(x_m,\ y_n)$, which is the primary signal intensity estimate.

$$A_{\rm f}(x_m,y_n) = A(I'_{\rm p}(x_m,y_n)/I_0(x_m,y_n))^{\alpha} \times(\ln(I_0(x_m,y_n)/I'_{\rm p}(x_m,y_n)))^{\beta}, \quad (3)$$

$$h_{\rm S}(x,y) = \exp(-(x^2+y^2)/2\sigma_1^2) +B\exp(-(x^2+y^2)/2\sigma_2^2). \quad (4)$$

Once we have obtained the blocked region, we can derive the estimates of $\alpha,\ \beta,\ A,\ B,\ \sigma_1,\ \sigma_2$ from the above equations. As we know, there might be different groups of parameters in different regions. Sun et al. [12] have performed some research on that scatter PSF parameter estimation using the model in Eq. (2) for three thickness groups.

Based on the idea presented above, the scatter kernel superposition (SKS) method is inherently iterative. A primary estimate is convolved with the scatter kernel to generate a new and refined scatter estimate which, in turn, is used to update the primary estimate.

2.4 Evaluation of scatter reduction and correction

To study the effects of direct scatter reduction and scatter correction for the proposed method, we compare the simulated projection images from the following two scenarios: (A) without the SDB or scatter correction; and (B) with the SDB and scatter correction, and CBCT images from the following three scenarios: (A) without the SDB or scatter correction (conventional CBCT); (B) with a fan-beam CT; and (C) with the SDB and scatter correction. We compare the three scenarios in terms of contrast-to-noise ratio (CNR) and the magnitude of cupping quantitatively. The CNR is analyzed by identifying two circular regions of interest (ROIs), one is within an insert material for analysis and the other as a reference in an adjacent normal phantom material region with similar distance to the phantom center. The CNR is calculated as:

$$\mathrm{CNR} = |u_{M,1}-u_{M,2}|/\sigma_M, \quad (5)$$

where $u_{M,1}$ and $u_{M,2}$ are the mean of the measured CT numbers of the ROIs in the insert and normal phantom material, respectively; $\sigma_{M,1}$ and $\sigma_{M,2}$ are the corresponding standard deviations of measured CT numbers. The voxel noise (σ_M) is calculated as $\sigma_M = (\sigma_{M,1}+\sigma_{M,2})/2$.

The error of the CT number in the ROIs is calculated as the square root of the mean square error, defined as:

$$E_{\rm RMSE} = \sqrt{\mathrm{mean}[(\mu_i-\overline{\mu}_i)^2]}, \quad (6)$$

where i is the index of the ROIs, $\overline{\mu}_i$ is the mean reconstructed value in Hounsfield uinside the ROIs, and μ_i is the corresponding value measured in the ground-truth image.

The magnitude of cupping is extracted in terms of the voxel values at the center $u_{M,\rm center}$ and edge $u_{M,\rm edge}$of the phantom. It can be defined as:

$$\tau_{\rm cup} = 100\times|u_{M,\rm edge}-u_{M,\rm center}|/u_{M,\rm edge}. \quad (7)$$

The original scatter of pixel (x,y) is $I_{\rm S}(x,y)$ and the resultant scatter estimation is $I'_{\rm S}(x,y)$. Before scatter correction the scatter-to-primary ratio (SPR) can be computed as follows:

$$F_{\rm SPR}(x,y) = \frac{I_{\rm S}(x,y)}{I_{\rm p}(x,y)}, \quad (8)$$

where $I_{\rm p}(x,y)$ is the scatter-free signal intensity at position (x,y).

Using the proposed scatter correction method, the corrected scatter to primary ratio ($\mathrm{SPR_c}$) can be computed as follows:

$$F_{\rm SPR_c}(x,y) = |I_{\rm S}(x,y)-I'_{\rm S}(x,y)|/I_{\rm p}(x,y). \quad (9)$$

2.5 Monte Carlo simulation

In the field of X-ray imaging, Monte Carlo simulation is an important tool. It gives the possibility of understanding the experimental results and it allows the construction of virtual imaging setups with predictions of their quality. Our approach is validated by comparing with the exact solution, while the latter is compared with the result from Monte Carlo simulations because numerous studies have demonstrated the accuracy of Monte Carlo simulations [4, 8, 9]. Open sources of the Monte Carlo code system are available such as Roentgen Simulation (ROSI) and EGSnrc [24]. They simulate the transport process

of photons and electrons in media, namely, the interaction of the particles with surrounding matter, and record the state history of each original particle and its descendants, including the retained energy, velocity, and position. Monte Carlo techniques use known interaction cross sections to simulate occurrences of various modeled interactions. With associated codes such as ROSI, one can build a simulated source-collimator-medium-detector system and study radiation interaction processes.

Our Monte Carlo user code is derived from the ROSI open source, which has been developed for investigating physical problems of X-ray imaging and designed for high simulation speed on common personal computers [24]. In this paper, we use ROSI to simulate the projection data of CBCT.

The simulation setup is defined: a phantom is imaged with an X-ray tube and a photon counting cadmium telluride detector.

An X-ray tube with a molybdenum anode, 2 mm aluminum prefiltering and a voltage of 120 keV is taken as the photon source. The detector is assumed to be an ideal gallium arsenide plate with a thickness of 1 mm and a size of 20 cm×20 cm.

The distance from the emission point of the X-ray source to the detector is set to 60 cm. The box is placed 10 cm in front of the detector (see Fig. 2).

In order to simulate a photon counting detector, a two dimensional histogram is defined. For this simulation 200×200 bins are defined. This means that each pixel has a size of 1 mm×1 mm. After a photon is absorbed in the detector the coordinate of the absorption point is read out. According to the coordinates the content of the appropriate bin is increased by one.

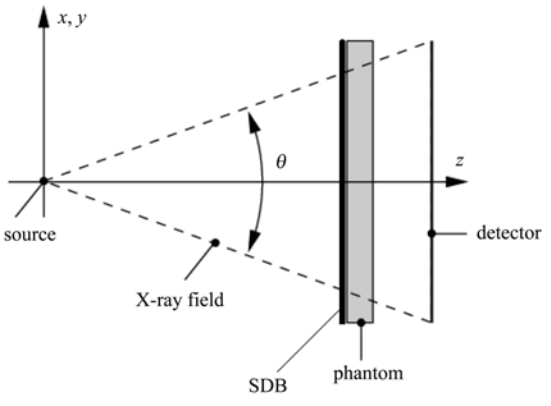

Fig. 2. The principle setup of the example.

2.6 The tabletop CBCT system

The parameters of the tabletop CBCT system used in this work are summarized in Table 1. The geometry of the system is conceptually equivalent to that of a clinical CBCT system, except that the phantom is rotated, which provides an ideal circular trajectory. The system in the laboratory consists of a Varian G-1590SP X-ray tube, a rotation stage, a Varian PaxScan 4030CB flat panel detector, and a workstation. The X-ray tube has an inherent filtration of 1.0 mm Al, 12° target angle, and operates with a 0.6 mm nominal focal spot size. No bow-tie filter or anti-scatter grid is used on this system. We mount the attenuation modulator on the outside surface of the collimator, with a nominal distance to the X-ray focal spot of 230 mm. In addition, the method is evaluated on tabletop Feldkamp Davis Kress (FDK) based CBCT systems.

Table 1. Imaging parameters of the physical experiments.

parameter	system value
X-ray focal spot	0.6 mm
X-ray energy	120 keV
detector size	0.388 mm×0.388 mm, 1024×768 pixels
source-to-imager distance	1400 mm
source-to-object center distance	1000 mm
source-to-modulator distance	230 mm
anti-scatter grid	No
bow-tie filter	No

3 Results

3.1 Monte Carlo simulation

Phantom Ⅰ: a box (20 cm wide ×20 cm long ×8 cm in thick) consists of polymethyl methacrylate (PMMA). In Fig. 3(a), the result of a simulation with 5×10^7 photons is shown. The scatter artifacts are greatly reduced in the images using the proposed method, which can be seen in the Fig. 3(c). The simulated projection image after scatter correction and data interpolation (in blocked regions) is show in Fig. 3(d).

Our approach reduces the τ_{cup} from 26.09% to 1.26% and increases the error of the CT numbers only from 11% to 16%. The mean of the original F_{SPR} is 21%. After scatter correction, the mean F_{SPR_c} is 1.4%, and the maximum F_{SPR_c} is 4%. It can be seen that the proposed scatter correction method works well.

Phantom Ⅱ: the phantom is mainly out the of water containing filled rods and is placed in a box (20 cm wide ×20 cm long ×8 cm in thick). Each rod has a length of 8 cm and a diameter of 5 cm. The rods' materials are show in Fig. 4(a).

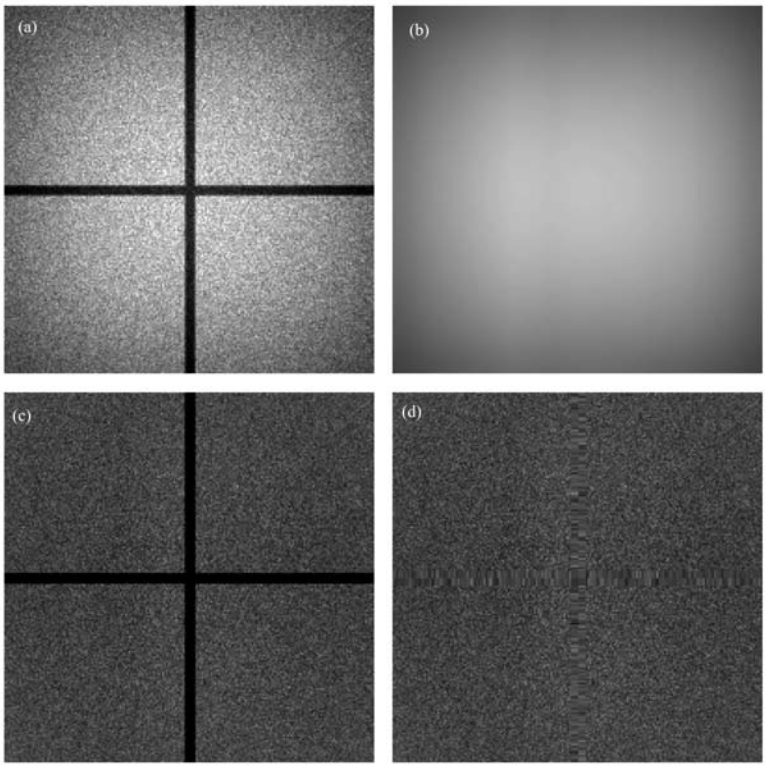

Fig. 3. (a) A simulated photon counting picture; (b) The scatter distribution using our method; (c) The simulated projection image with scatter correction; (d) The simulated projection image after scatter correction and data interpolation.

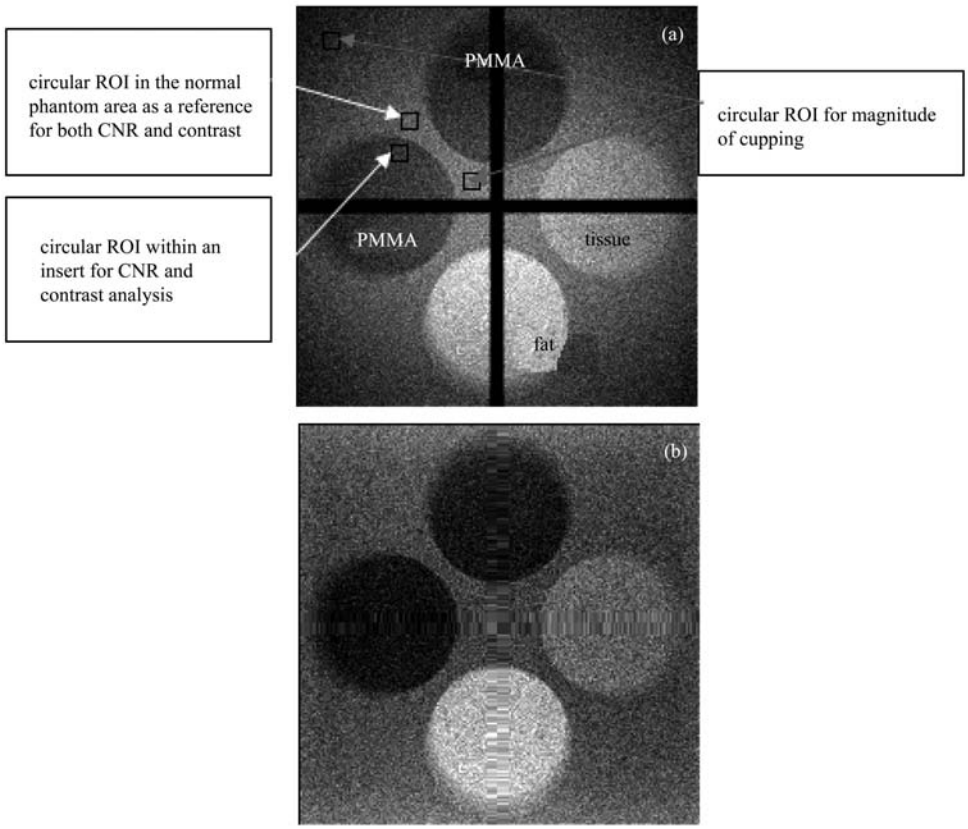

Fig. 4. (a) A simulated photon counting picture and the selected ROIs; (b) The simulated projection image after scatter correction and data interpolation.

Table 2. A quantitative analysis of Phantom Ⅱ. Projection image without scatter correction (PI NONE), projection image with scatter correction (PI SC), Sun's method [12] (SKS).

modality	E_{RMSE}(edge)	E_{RMSE} (center)	contrast	CNR	τ_{cup} (%)	mean SPR (%)
PI NONE	34.01	28.04	86.04	2.55	16.47	14.2
PI SC	34.50	27.37	105.09	3.20	5.95	3.1
SKS	34.47	26.25	100.15	2.99	13.07	7.0

In Fig. 4(a), a simulation result of 5×10^8 photons is shown. The simulated projection image after scatter correction and data interpolation (in blocked regions) is shown in Fig. 4(b). A quantitative analysis of Phantom Ⅱ is given in Table 2.

3.2 Generating CBCT images

Figure 5 shows the reconstructed images. The image distortion (cupping, etc.) due to the scatter is obvious in the reconstructed image without scatter correction (a). The scatter artifacts are greatly reduced in the images using the proposed method, which can be seen in (c). CT acquired in fan beam geometry is shown in (b).

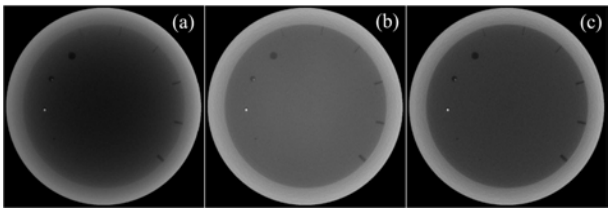

Fig. 5. Image reconstructions of the phantom. (a) CBCT without scatter correction; (b) CT acquired in fan beam geometry; (c) CBCT with scatter correction.

The 1D horizontal profile with and without scatter signals can be seen in Fig. 6. From the figure, we can see that the theory of the proposed method is similar to the fan beam result.

We measure the CNR and τ_{cup} in the selected ROIs in Fig. 7. The result can be found in Table 3.

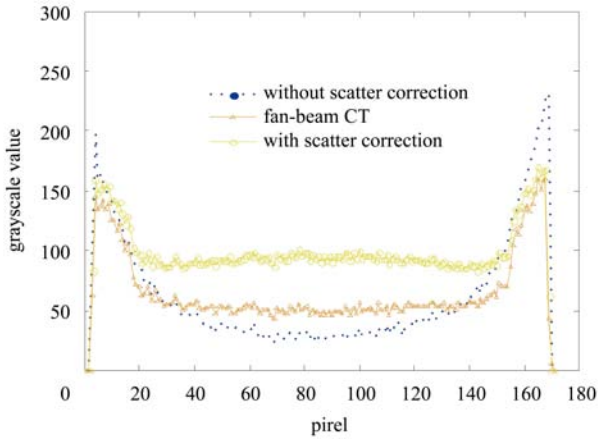

Fig. 6. The 1D horizontal profile of the measured and estimated scatter signals on the phantom: the column shows the profiles of the projected images which are at row 256 in Fig. 5.

Table 3. The quantitative image quality investigation for different modalities: CBCT without scatter correction (CBCT NONE), CBCT with scatter correction (CBCT SC), fan beam geometry (FBCT).

modality	τ_{cup} (%)	CNR
CBCT NONE	41.76	2.94
FBCT	4.78	3.53
CBCT SC	9.13	3.31

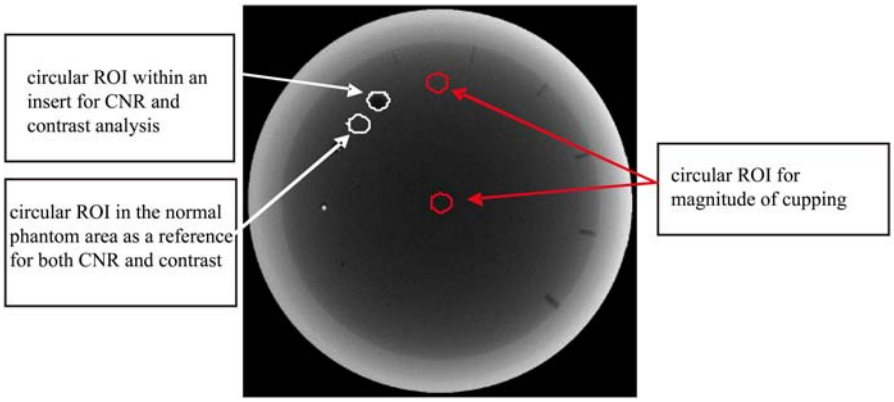

Fig. 7. Illustration of the method for quantitative analysis of image quality. The left shows two circular ROIs, one within an insert material for analysis and the other in an adjacent normal phantom material region with a similar distance to the phantom center, are marked for analyzing CNR and contrast. The right two ring ROIs, one around the edge and the other in the center, are used as the magnitude of cupping analysis.

4 Discussion

SKS offers a practical and real-time method to estimate and subtract scatter from cone-beam projection data but has been considered to be insufficiently accurate for many applications. To address this weakness, we have developed the techniques using SDB that model the self-adaptive scatter kernel. Our comprehensive approach addresses the differential attenuation of scatter due to local thickness changes. The results show that the method offers significant improvements compared with the previous scatter kernel method.

The result shows that our algorithm produces substantial image quality improvements. The proposed method provides combined scatter correction and direct scatter reduction. Scatter correction eliminates the scatter artifacts, but may slightly degrade the CNR, while direct scatter reduction improves the CNR to compensate the CNR degradation from scatter correction. An improvement of the CNR is observed for the specific setting in this study. This is an improvement in comparison with the previous techniques, in which the CNR is usually degraded. In addition, the magnitude of cupping is greatly reduced. Referring to Table 2, the τ_{cup} is reduced from 16.47% to 5.95%.

5 Conclusion

The accuracy of the SKS technique can be significantly improved in our method, which uses self-adaptive scatter kernel superposition. The result shows that our algorithm produces substantial image quality improvements. The proposed comprehensive approach also addresses the scatter PSF broadening resulting from object thickening, object edge effects, detector scatter properties, and an anti-scatter grid.

In the future, different SDB and kernel models should be designed to investigate the impact of scatter distribution on the scatter correction performance.

The authors wish to thank the anonymous referees for their constructive and insightful comments, which greatly improved this paper.

References

1 Boone J M, Seibert J A. Medical Physics, 1988, **15**: 721
2 Floyd Jr C E et al. Investigative Radiology, 1993, **28**(5): 427
3 Siewerdsen J et al. Medical Physics, 2006, **33**: 187
4 YAO W, Leszczynski K W. Medical Physics, 2009, **36**: 3145
5 YAO W, Leszczynski K W. Medical Physics, 2009, **36**: 3157
6 Maltz J S et al. Medical Imaging, IEEE Transactions on, 2008, **27**(12): 1791–1810
7 LI H, Mohan R, ZHU X R. Physics in Medicine and Biology, 2008, **53**: 6729
8 Mainegra-Hing E, Kawrakow I. Fast Monte Carlo Calculation of Scatter Corrections for CBCI Images [c]. Phys.: Conf. Ser. 102. IOP Publishing, 2008
9 Poludniowski G et al. Physics in Medicine and Biology, 2009, **54**: 3847
10 Rinkel J et al. Physics in Medicine and Biology, 2007, **52**: 4633
11 Spies L et al. Medical Physics, 2000, **27**: 462
12 SUN M, Star-Lack J. Physics in Medicine and Biology, 2010, **55**: 6695
13 NING R, TANG X, Conover D. Medical Physics, 2004, **31**: 1195
14 ZHU L, Strobel N, Fahrig R. X-ray Scatter Correction for Cone-Beam CT Using Moving Blocker Array. 2005
15 Bani-Hashemi A et al. Med. Phys., 2005. **32**(6): 2093
16 Persliden J, Carlsson G A. Physics in Medicine and Biology, 1997, **42**: 155
17 Floyd Jr C E, Chotas H G, Ravin C E. Investigative Radiology, 1994, **29**(9): 852
18 Graham S et al. Medical Physics, 2007, **34**: 2691
19 ZHU L, WANG J, XING L. Medical Physics, 2009, **36**: 741
20 ZHU L et al. Medical Physics, 2009, **36**: 2258
21 CAI W, NING R, Conover D. Optical Engineering, 2008, **47**: 097003
22 YAN H et al. Physics in Medicine and Biology, 2010, **55**: 6353
23 ZHU L, Bennett N R, Fahrig R. Theory and Preliminary Results. Medical Imaging, IEEE Transactions on, 2006. **25**(12): 1573–1587
24 Giersch J, Weidemann A, Anton G. Nuclear Instruments and Methods in Physics Research Section A: Accelerators, Spectrometers, Detectors and Associated Equipment, 2003, **509**(1–3): 151–156